Optimizing Specific Actuation Force of Soft Composite Pneumatic Artificial Muscles Using Additively Manufactured Components

Christopher Clark, Frank Cianciarulo Dr. Norman Wereley

Optimizing Specific Actuation Force of Soft Composite Pneumatic Artificial Muscles Using Additively Manufactured Components

Christopher Clark, Frank Cianciarulo, and Norman Wereley

Composites Research Laboratory, University of Maryland, College Park MD 20742

Abstract

Pneumatic artificial muscles (PAMs) are composite actuators comprised of a Kevlar braid, latex bladder, and two aluminum end-fittings through which inflation, deflation, and transfer of external loads can be achieved. PAMs can exhibit extensile or contractile forces based on the choice of braid angle. PAMs show exceptional specific actuation force when normalized by their weight. However, the end fittings are typically machined from aluminum. Lighter materials, such as Acrylonitrile Butadiene Styrene (ABS-R), could be used to reduce the weight of the end-fittings and increase the specific actuation force. This research focuses on the design, fabrication, and testing of contractile PAMs for which aluminum end fittings are replaced with lightweight 3D-printed end fittings. 3D-printed PAMs were tested under quasi-static axial loads for a range of inflation pressures. PAMs were tested in blocked force and free contraction using a Materials Testing System (MTS) servo-hydraulic testing machine. Burst and actuation testing was conducted to determine the PAM's maximum failure load, and fully characterize their output force with respect to percent contraction. A 120-psi burst pressure was chosen to provide a safety factor of 1.2 when operating the PAM between 0 and 100 psi. PAMs tested in actuation were cycled quasi-statically between normal operating pressures from blocked force to free contraction. After additive manufacturing and design alterations, the PAMs burst pressure was improved from 363 lbf at 43 psi to 1160 lbf at 123 psi, showing their ability to withstand large axial forces within the specified pressure limits. 3D-printed PAM actuation characteristics show comparable performance to PAMs built using aluminum end fittings and show no loss in force per unit contraction when switching from aluminum to 3D-printed end fittings.

Keywords: Pneumatic artificial muscles, 3D printing, Burst test, Actuators, Composite Actuators

1 Introduction

Pneumatic artificial muscles (PAMs), when inflated with a working fluid such as air, expand or contract based on the configuration of their braiding. Contractile PAMs experience radial expansion of the braid and bladder as they inflate. This resulting radial expansion produces contraction in the axial direction which contributes to a large axial actuation force. The ability of PAMs to generate these large axial forces all while being lightweight makes them well-suited for actuation applications involving high specific actuation force and specific power [1, 2, 3, 4, 5], with work spanning into aerospace and robotics with trailing edge flap control [6, 7, 8] and biomimetics [9, 10]. Their lightweight and high force output characteristics allows for a competitive edge over other commonly used mechanical and hydraulic actuators. PAMs are typically made using aluminum end-fittings. For industries looking to improve the actuation characteristics of PAMs, ABS-R can be used to increase the specific actuation force of PAMs through weight reduction. Using the standard swaging techniques for metallic end fittings by using a compression fitting and binding the assembly with epoxy [8], 3D-printed end fittings can be constructed and implemented in a similar fashion, while matching the actuation performance of metallic PAMs. The main goal of this study is to develop 3D-printed PAMs using lightweight ABS-R where, via weight reduction, specific actuation force can be maximized. To do this, 3D-printed PAMs were developed where the PAMs would have to operate within a specified pressure range

of 0-100 psi, all while also ensuring a safety factor of 1.2 where a maximum pressure without burst of 120 psi must be achieved. An actuation diagram is constructed to analyze the 3D-printed PAM performance while axially loaded and a comparison is made between 3D-printed PAMs and metallic PAMs.

2 Fabrication

To maximize PAM actuation characteristics, particularly specific axial contraction force, replacing aluminum end-fittings with ABS-R and introducing a weight reduction while maintaining axial contraction force is required. 3D-printed end-fittings contain two components, the inner end-fitting and end-fitting socket, both of which combine to create a full PAM end-fitting. To develop a full 3D-printed end-fitting, the inner end-fitting and end-fitting socket were printed using a MakerBot Method X, which prints by way of fused deposition modeling. The MakerBot Method X supports various types of filaments, but for the development of the end-fittings, high strength tolerance was preferred, therefore ABS-R was chosen. ABS-R plastic is an ABS-based filament developed by MakerBot which has improved print reliability and refined jam reduction. The end-fittings are also printed with SR-30 support material, a liquid-soluble support material used exclusively with high-temperature filaments. For the inner end-fitting, the height is 0.95", the inner diameter is 0.39" and the outer diameter is 0.91". The end-fitting socket has a height of 1.19", inner diameter of 0.98", and an outer diameter of 1.29".

Specific axial contraction force maximization comes from the difference in material density between ABS-R and aluminum where ABS-R filament has a density of 1.0 g/cm^3, and aluminum has a density of 2.71 g/cm^3. Figure 1 presents a schematic for 3D-printed PAMs with a target active length of 12".

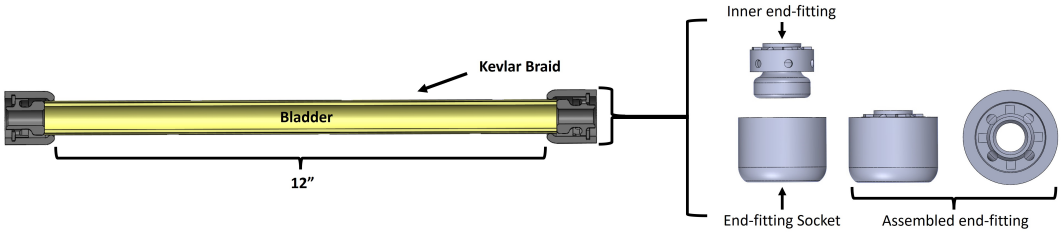

Figure 1: 3D-printed PAM Schematic

As mentioned before, PAMs consist of a Kevlar braid, latex bladder, inner end-fitting, and end-fitting socket. Figure 2 shows the PAM components.

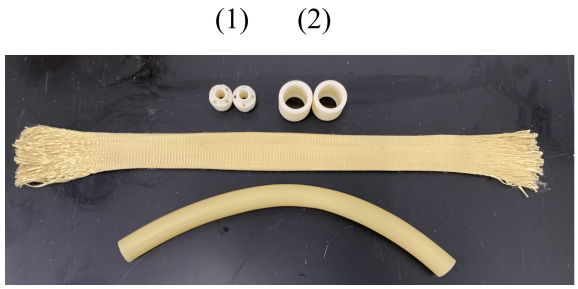

Figure 2: PAM components: Inner end-fittings (1), end-fitting sockets (2), Kevlar braid (3), latex bladder (4)

To construct a 3D-printed PAM, we start by cutting the kevlar braid and latex bladder to length. The PAMs utilized in this paper are twelve inches in active length, measured from the bases of the end-fittings. Further down the line when manufacturing the PAM, we will need to utilize the braid and hold it tight to assist in sliding the end-fitting sockets over the inner end-fittings. Therefore it is recommended to cut the braid longer than the intended PAM length. For a foot-long PAM, 5" of extra braid was added to each side

of the PAM. The full end-fittings are 0.75” of an inch in length, so to ensure extra braid on either side of the PAM, 1.50” plus 10” was added to the initial 12” cut length of the braid. For a foot-long PAM, the bladder was cut to 13.50”, 1.50” over the PAMs intended length to account for the length of the end-fittings. After cutting the braid and bladder to length, the next step is to insert the bladder into the braid and attach the inner end-fittings and end-fitting sockets. To do this, we’ll place the bladder centered inside the braid, then attach the end-fitting sockets by sliding them over the braid and bladder. The sockets are then pushed close to the center of the braid and bladder, allowing the inner end fittings to be attached to the ends of the bladder. Next, tightly secure one end of the PAM’s braid and pull the socket over the opposite end’s inner end-fitting. The inner end-fitting and end-fitting socket are held together through a compression fitting. West Systems epoxy resin 105-B and soft hardener 206-B are used to seal the connection between the braid, bladder, and end-fitting components. The same fabrication method is applied to the other side of the PAM after the epoxy has dried. Once the epoxy has dried on both sides of the PAM, the extra braid is cut from the PAM, and the PAM is threaded using a 7/16” tap. A diagram of the assembly process is shown below in Figure 3

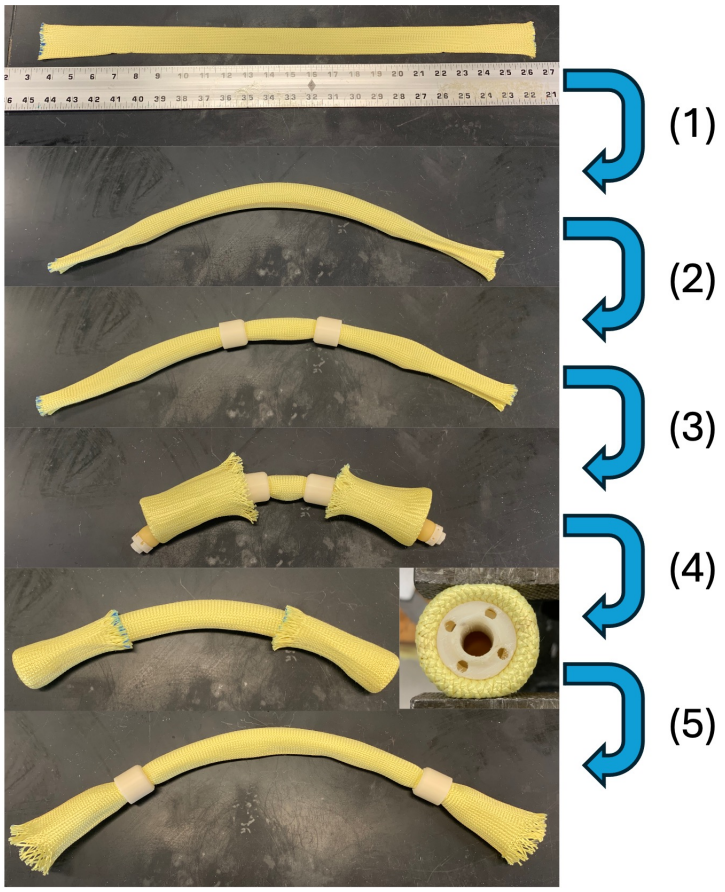

Figure 3: 3D-printed PAM assembly process

Figure 3 shows the steps for assembly of the 3D-printed PAM. Step 1 placing the latex bladder inside the braid, step 2 shows sliding the end-fitting sockets over the braid and bladder. Step 3 shows attaching the inner end-fitting to the ends of the bladder. Step 4 shows pulling the sockets over the inner end-fittings along with the setup for epoxying the end-fitting. The holes shown in step 4 are where epoxy is inserted by syringe to seal the inner end-fitting, end-fitting socket, braid and bladder together. Lastly, step 5 shows the epoxied end-fittings and extra braid ready to be trimmed.

3 Testing Procedure

Testing was conducted in two stages for the 3D-printed PAMs. Initial testing included burst testing to ensure the PAM could operate in the specified operating range of 0 to 100 psi and not burst at pressures less than 120 psi. The second stage of testing involved testing the 3D-printed PAM in quasi-static actuation to fully characterize the PAM at given pressures.

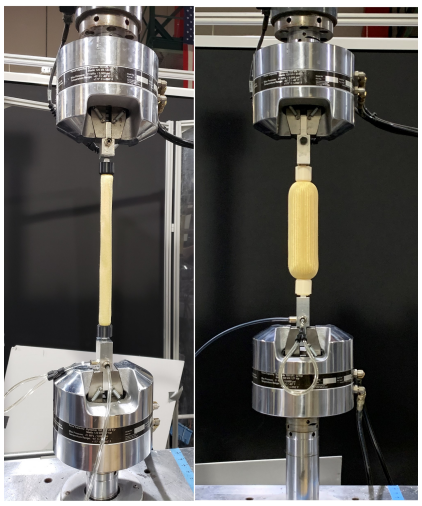

Figure 4: PAM setup: Left: PAM at blocked force during burst test. Right: PAM at free contraction during actuation cycling.

3.1 Burst Test

To test the PAM's maximum burst pressure and ensure the PAMs can operate within the specified operating range, the PAM is placed into a Materials Testing System (MTS) servo-hydraulic testing machine at resting length. The MTS collects axial contraction force and pressure for the duration of the test. The burst test is conducted with the PAM held at blocked force, so as the PAM begins to inflate, its ability to contract is prohibited, generating the maximum possible axial contraction force for each given pressure. The pressure is then brought up slowly while closely observing the PAM's behavior as pressure and axial contraction force increase. A successful test involves bringing the PAM up from 0 psi to 120 psi, and back down to 0 psi without failure.

3.2 Actuation Test

To fully characterize the 3D-printed PAMs, actuation testing was conducted to determine the PAM performance at specified pressures and their accompanying axial contraction force. To do this, the PAM is clamped into the MTS at resting length. With the PAM in place, the pressure is increased to 10 psi and cycled 3 times from block force to free contraction. Actuating the PAM before testing allows for the stiff uncycled elastomeric bladder to stretch within the PAM, a phenomenon known as the Mullins effect[11]. After cycling the PAM from blocked force to free contraction 3 times, the MTS is used to cycle the PAM at a quasi-static speed of 0.02 in/s. The PAM is tested quasi-statically to dismiss any damping forces applied to the PAM. This procedure of cycling the PAM from blocked force to free contraction three times, then testing the PAM for a total of three actuation cycles is carried out for all pressures in increments of 10 psi ranging from 10 to 100 psi.

3.3 Pressurization System

To actuate the PAMs during testing, a PID-controlled pressure system is used. The PID controller regulates and holds the pressure at a given psi within the PAM during actuation. The pressurization system uses a DEWALT Heavy-Duty 200 PSI 4.5 Gallon Electric Wheeled Compressor (D55146) to supply air to the system. The compressed air then travels to a Norgren R73G-3AT-RSG Pressure Regulator that allows for direct airflow control of the pneumatics entering the system. Air is then fed to an Enfield LS-V05s High Speed 5/3 Proportional Directional Valve which is powered by an Enfield D1 Bi-Directional Proportional PWM Valve Driver. The valve driver is then connected to an Agilent Dual Output 0-8V.5A/0-20V,2.5A DC Power Supply (E3648A), and an Arduino MEGA 2560 Rev3 Microcontroller which is connected to an operating computer that powers the Arduino. The direct proportional valve allows for full control of pneumatics entering the PAM at any given time. Air is then passed through an Omegadyne PX20 Pressure Transducer which reads the pressure in the PAM and feeds the information back to the microcontroller, which is then fed to the operating computer. The pressure transducer is also connected to the MTS which allows for pressure to be recorded alongside the axial contraction force and displacement.

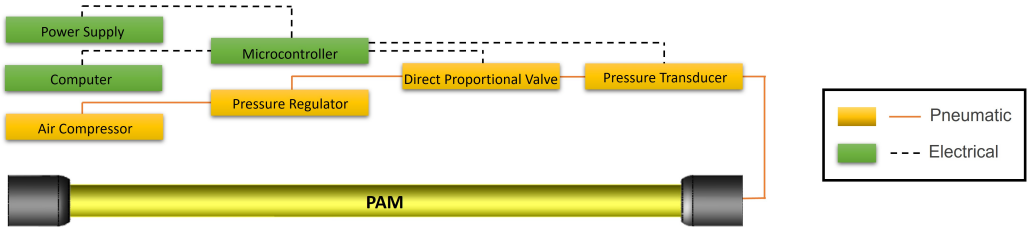

Figure 5: Pressurization System

4 Design Iterations and Burst Test Results

The first iteration 3D-printed PAM was printed with 20 percent infill density on the inner end-fittings and end-fitting sockets. The infill density of a 3D-printed component is a measure of the percentage of modeling material inside a 3D-printed part. Both components also include the use of 2 shells and utilize a balanced print mode. Shells on a 3D-printed part are the number of outside layers used on the model. A balanced print mode is a setting on the MakerBot Method X that prioritizes a balance between surface quality and print time. With the first 3D-printed PAM developed, burst testing was conducted.

Figure 6 shows the results from the first burst test of the 3D-printed PAM. The end-fittings failed at an axial force of 363 lbf at 43 psi. Due to the end-fittings failing within the expected operating range, we need to implement design changes to increase their performance. After a close examination, it was evident that one of the end-fittings failed due to delamination, and that half of the inner end-fitting component was ripped out of the end-fitting socket. Figure 7 shows the PAMs end-fitting after the first burst test.

During the 3D printing process, the orientation on which parts are printed plays a role in their capabilities. When the inner end-fitting was printed, it was printed from bottom to top with the component standing straight up. This made the layer lines of the print fall perpendicular to the direction of the applied axial force. Thus, causing the inner end-fitting to fail simply because the layers were separated during loading.

To combat delamination, print settings, and print orientation were adjusted. Instead of printing the inner end-fitting standing straight up, they were adjusted to be printed lying on their side, allowing the layer lines of the print to fall in the axial direction with the direction of the force. In addition to changing the printing orientation, an infill density increase from 20% to 70% was added. Increasing the infill density of the inner end-fitting allowed for more material to be used within the part, thus increasing its strength. With these new changes implemented, a second burst test was conducted.

The end-fittings failed at an axial force of 559 lbf at 68 psi due to inner end-fitting pull-out rather than previously seen delamination. The inner end-fitting pull-out is a result of the compression fitting between the inner end-fitting and end-fitting socket along with the epoxy being unable to hold the inner end-fitting in place. Figure 9 shows the inner end-fitting pullout from the end-fitting socket

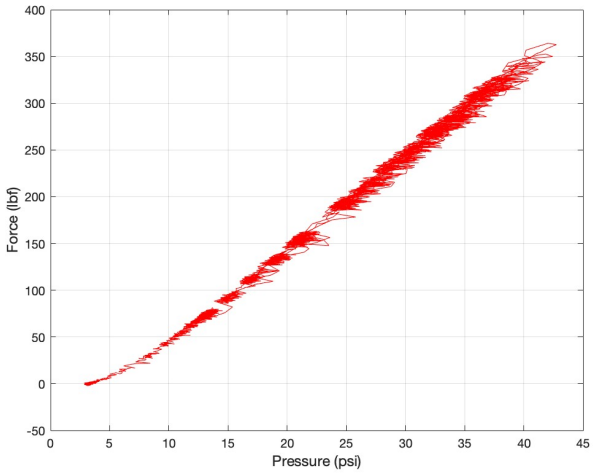

Figure 6: First iteration. Max pressure: 43 psi. Target pressure: 120 psi

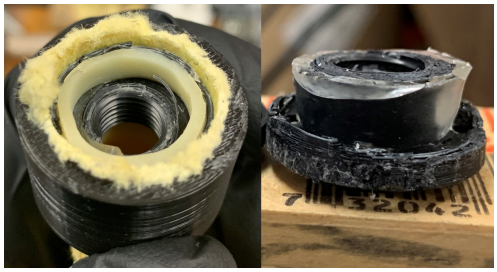

Figure 7: End-fitting delamination

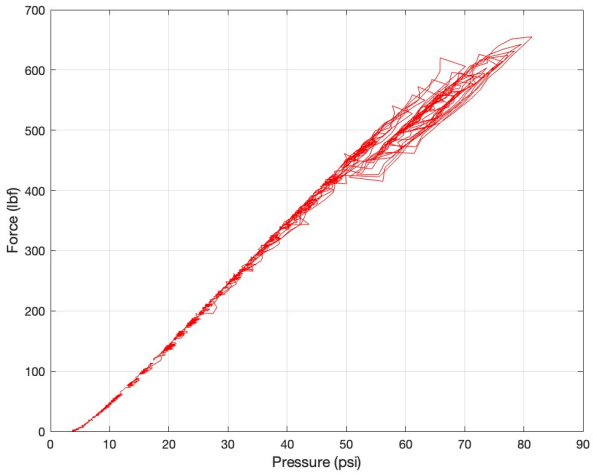

Figure 8: Second iteration. Max pressure: 68 psi. Target pressure: 120 psi

Figure 9: Inner end-fitting pullout from socket

During the process of manufacturing 3D-printed PAMs, there are two ways in which the inner end-fitting is secured into the socket. One is through a compression fitting between the inner end-fitting and end-fitting socket, and the other is through the application of epoxy, which is visible in Figure 8. Since the inner end-fitting was pulled directly from the socket while keeping the inner end-fitting intact, a retaining ring design was implemented to hold the inner end-fitting in place. For design iteration 3, we incorporated a 3D-printed retaining ring that sits over the top of the inner fitting and underneath the end-fitting socket. To do this, a cutout was introduced into the end-fitting socket which housed the retaining ring. The end-fitting socket dimensions were extended in the radial direction through an increase in diameter by 0.16". This extension allows for the retaining ring to sit 0.08" underneath the socket and leaves 0.16" in wall thickness for strength in the radial direction. Figure 10 shows the third iteration retaining ring end-fitting design.

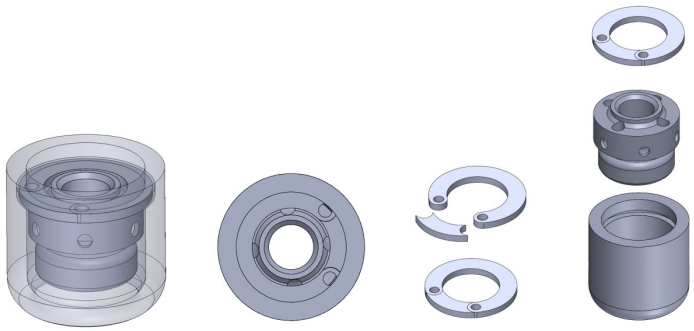

Figure 10: : Retaining ring end-fitting design: (1) Full assembly, (2) top-down view, (3) retaining ring components, (4) end-fitting components (retaining ring, inner end-fitting, and end-fitting socket).

It is worth noting that the retaining ring was printed using 20% infill density. Since the fabrication of the PAM involves compressing the retaining ring into the socket, high infill density increases the stiffness of the ring, causing the ring to break before it can be inserted into the cutout. Multiple prints of infill densities ranging from 20-40 percent and one being at 70 percent show the retaining ring breaking over 20 percent while inserting it into the cutout. Therefore the ring was printed with a 20 percent infill density to ensure it can be used in the end-fittings. The retaining ring has an inner diameter of 0.67" and an outer diameter of 1.06". With the new end-fitting design printed and the PAM manufactured, a third burst test was conducted. Figure 11 shows the results of the burst test conducted on the third iteration retaining ring PAM design.

The end-fittings failed at an axial force of 655 lbf at 81 psi. During the inspection of the PAM after testing, it was evident that the PAM failed due to thread detachment. The connection between the PAM and the MTS was removed and the PAM threads were observed to be stripped. Figure 12 shows the damage sustained by the threads on the inner end-fitting.

It was observed that when tapping the PAM's inner end-fittings, the threads were unable to dig into fully solid material. The threads would cut through the two shells of the print, and reach the portion of the inner end-fitting where the component was not solid. This made the outer shells of the threaded inner end-fitting where the MTS attachment is housed fall off. To combat thread failure, the amount of shells on the inner end-fitting was increased from 2 to 4. A change in the print mode for the components was also made. Instead of printing in balanced mode, MakerBot provides a solid print mode option that prints highly dense and stronger 3D prints. This change was implemented to maximize the density of the inner end-fitting to avoid damage to the threads. Additionally, the top edge of the inner end-fitting where the MTS is attached was raised by 0.12". This allows for more epoxy to sit on top of the retaining ring, providing more resistance against an inner end-fitting pullout. Figure 13 shows the fourth iteration PAM end-fittings.

With the new changes implemented, a fourth iteration of 3D-printed PAM was developed and burst-tested. Figure 14 shows the combined results for iterations 1-4. The fourth burst test with the new manufacturing changes experienced no failure and reached a force of 1160 lbf at 123 psi. This test shows that the retaining ring design can reach the required pressure of 120 psi without failure, ensuring a safety factor of 1.2.

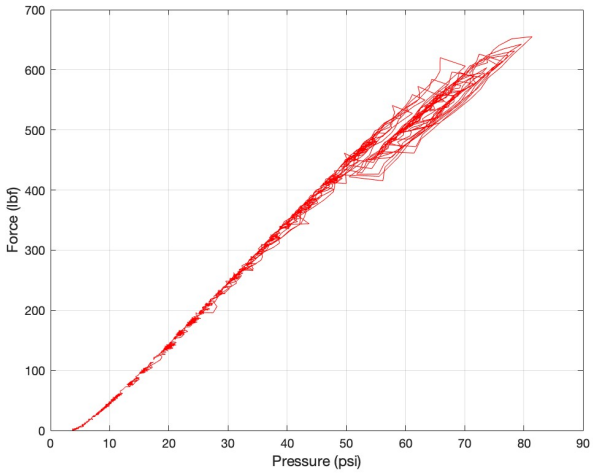

Figure 11: Third iteration. Max pressure: 81 psi. Target pressure: 120 psi

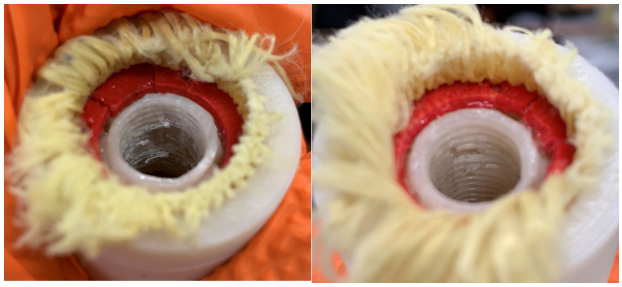

Figure 12: Thread failure on third iteration PAM

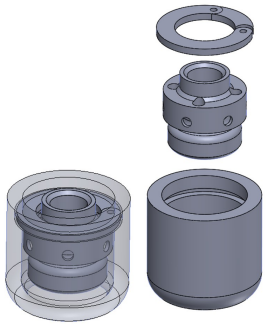

Figure 13: Fourth iteration PAM design full end-fitting

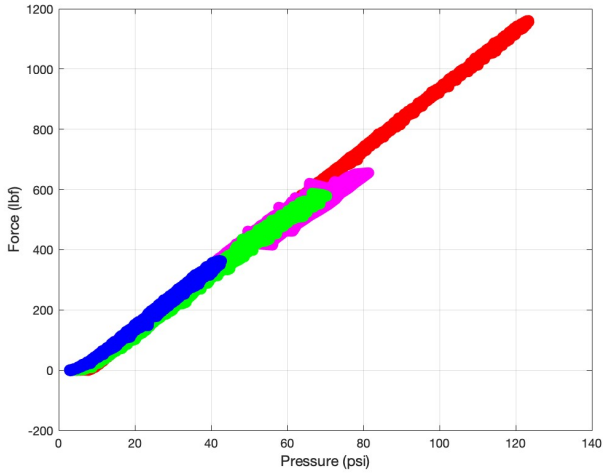

Figure 14: Iterations 1-4 burst data. blue: iteration 1, green: iteration 2, magenta: iteration 3, red: iteration 4

5 Actuation Test and Analysis

With a 3D-printed PAM design now able to reach the required safety factor of 1.2, an actuation test was conducted to characterize the PAM from 10-100 psi.

5.1 Actuation Analysis

A PAM model adapted from Ref [12] was used to model the actuation properties of both the 3D printed and metallic PAMs. To model the PAMs, the number of turns of the braid, N, and the braid length, B, were first found as follows:

$$N = \frac{L_0}{D_0 \pi tan(\theta_0)} \tag{1}$$

$$B = \frac{L_0}{sin(\theta_0)} \tag{2}$$

where D_0 is the outer diameter of the PAM, θ_0 is the initial braid angle, and L_0 is the initial length. The Gaylord force is determined using

$$F_{Gaylord} = \frac{P}{4\pi N^2}(3L^2 - B^2) \tag{3}$$

The Gaylord force, from Eq. 3, is useful for predicting the blocked force of the PAM where little energy from inflation is being utilized to stress the bladder. For actuation states with significant bladder strain, a more comprehensive model is required.

First, the diameter of the PAM as a function of the PAM length is defined in eq. 4 and the instantaneous braid angle is defined below:

$$D(L) = \frac{\sqrt{B^2 - L^2}}{\pi N} \tag{4}$$

$$\frac{cos(\theta_1)}{D_1} = \frac{cos(\theta_2)}{D_2} \tag{5}$$

As the PAM inflates, the bladder is strained both circumferentially and axially. These strains are defined by equations 6 and 7, respectively.

$$\epsilon_c = \frac{R}{R_0} - 1 \tag{6}$$

$$\epsilon_z = \frac{L}{L_0} - 1 \tag{7}$$

Due to the hyperelastic nature of the bladder, the stresses in the bladder were modeled using a fourth-order relationship between stress and strain

$$\sigma_c = \sum_{k=1}^{4} E_k \epsilon_c^k \tag{8}$$

$$\sigma_z = \sum_{k=1}^{4} E_k \epsilon_z^k \tag{9}$$

where σ_c is the circumferential stress, Eq. 8, and σ_z is the axial stress, Eq. 9.

Using these formulations, the complete axial model for the PAM can be written as:

$$F = \frac{P}{4\pi N^2}(3L^2 - B^2) + \sigma_z \frac{V_B}{L} - \sigma_c \frac{tL^2}{2\pi R N^2} \tag{10}$$

where P is the internal pressure, L is the length of the PAM, V_B is the volume of the bladder, t is the bladder thickness, and R is the PAM radius.

The optimization problem used to determine the moduli of the bladder can be written as:

$$\begin{aligned} \min_{x} \quad & \sum_{k=1}^{n} \sqrt{\frac{\sum_{i=1}^{m} (F_{M,i,k} - F_{E,i,k})^2}{m}} \\ \text{s.t.} \quad & lb \leq x \geq ub \\ & c(x) \leq 0 \end{aligned} \tag{11}$$

where F_M is the force predicted by the model, F_E is the measured experimental force, m is the total number of data points taken for a given pressure, and n is the total number of pressures tested. The variable x being optimized is a vector comprised of $[x_1, x_2, x_3, x_4, x_5, x_6, x_7, x_8]^T$. These variables are used to determine the moduli in the form of

$$\begin{aligned} E_1 &= x_1 P + x_2 \\ E_2 &= x_3 P + x_4 \\ E_3 &= x_5 P + x_6 \\ E_4 &= x_7 P + x_8 \end{aligned} \tag{12}$$

The lower bounds on x are $\{x_k = -1000 \,|k = 1, ..., 8\}$ while the upper bounds are $\{x_k = 1000 \,|k = 1, ..., 8\}$. Finally the non-linear constraint, $c(x)$, can be defined as

$$c(x) = -(dE_c + dE_z) \tag{13}$$

where dE_c is the incremental internal circumferential energy and dE_z is the incremental internal axial energy. This constraint comes from the Drucker stability criteria, which states that the incremental internal energy of a stable material must increase as strain increases.

5.2 Actuation Results

Using the complete axial model and bladder moduli optimization, an actuation diagram was constructed using data obtained from actuation testing from 10-90 psi. Figure 15 shows the axial force output with respect to percent contraction at specified pressures from 10-90 psi.

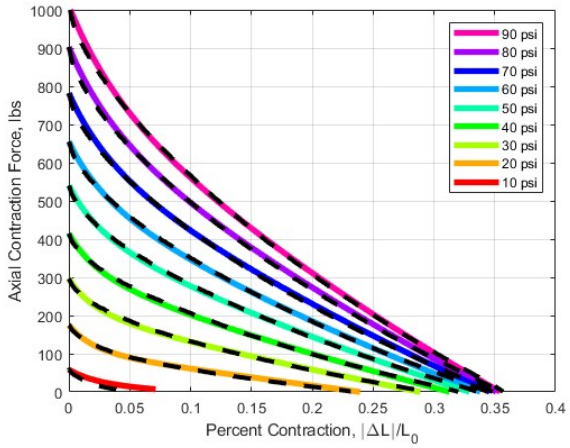

Figure 15: 3D-printed PAM actuation diagram

5.3 Actuation Test

During the manual cycling portion of the test, the PAM experienced delamination to a section of the end-fitting socket at 100 psi. Therefore actuation data from 10-90 psi was only able to be obtained. Figure 16 shows the damage sustained by the end-fitting socket during actuation.

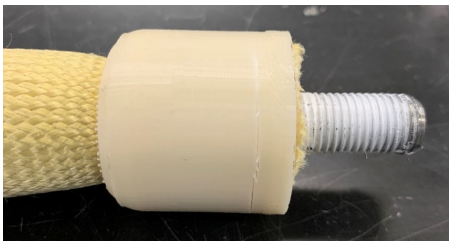

Figure 16: End-fitting Socket delamination

The placement of the delamination showed that the cause of the failure was due to the retaining ring pulling on the end-fitting socket axially. This axial load is a result of the retaining ring sitting inside the end-fitting socket, where it holds the inner end-fitting in place. The resulting new load begins to pull the socket apart which was designed to handle high radial forces, not high axial forces. The layer lines of the end-fitting socket lay perpendicular to the new axial load, making it prone to failure by delamination, similar to the failure seen in the first iteration of 3D-printed PAM.

6 PAM comparison

With actuation characterized for 3D-printed PAMs, a comparison between 3D-printed and metallic PAMs can be made to observe their performance in actuation with a change in end-fitting design. A comparison at 30, 60, and 90 psi was made to examine their actuation capabilities through the range of pressures tested. The metallic PAM used to provide the actuation diagram was 12.63" in length and the 3D-printed PAM was 11.875" in actual length. The 3D-printed PAM weighed 0.17 *lbs*, and the metallic PAM weighed 0.22 *lbs* Figure 17 shows the actuation diagrams for 3D-printed and metallic PAMs.

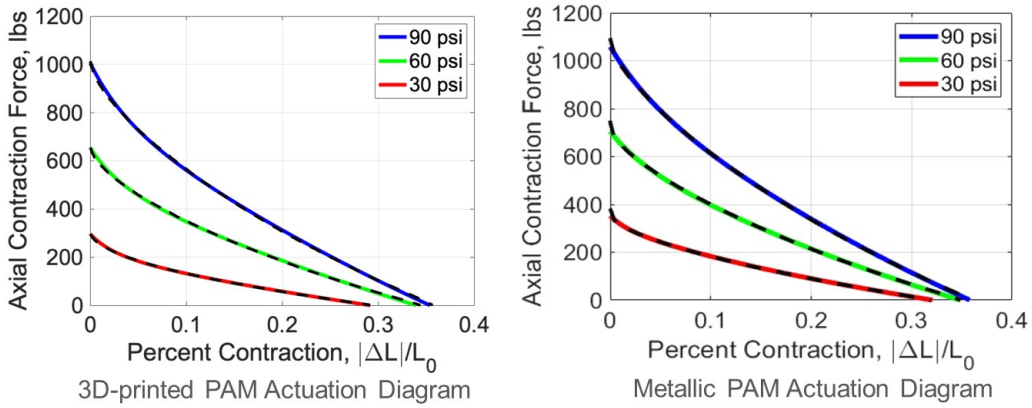

Figure 17: PAM actuation diagrams for PAMs with 3D-printed (left) and metallic (right) end fittings

A comparison between 3D-printed and metallic PAMs shows a slight difference in axial contraction force at 30, 60, and 90 psi. This axial contraction force difference is a result of a slight dissimilarity between the 3D-printed and metallic braid angles, with the metallic PAM braid angle measuring 73 degrees, while the 3D-printed PAM measured 71 degrees. With a difference in braid angle θ_0, we can see an increase in axial contraction force based on the N component increasing and the B component decreasing in the Gaylord

force equation due to equations 1 and 2 respectively. This in turn explains the variance between 3D-printed and metallic PAMs. Ultimately, with the slight axial contraction force difference, an actuation comparison still shows the 3D-printed PAM matching the performance of metallic PAMs. Without adjusting the axial contraction force, we can use the data from Figure 17 to find the specific actuation force. At 30 psi, the 3D-printed PAM lagged behind the metallic PAM with a 5% decrease in specific actuation force. At 60 psi there was an increase by 7% in the specific actuation force, and at 90 psi there was an increase by 11%.

7 Conclusion

PAM specific actuation force was maximized in this study through a reduction in the weight of their end-fittings. By replacing typical aluminum end-fittings with 3D-printed ABS-R plastic, we were able to show that 3D-printed PAMs can match the performance capabilities of metallic PAMs, all while maintaining the nominal axial contraction force seen in the metallic PAMs. 3D-printed and metallic PAMs were compared through their specific actuation forces using data from Figure 17 and their total weights. The 3D-printed PAMs showed a higher specific actuation force at 60 psi where there was an increase by 7%, and 90 psi where there was an increase by 11%. 3D-printed PAMs were developed and tested in blocked force, where multiple failure modes were examined. End-fitting delamination in iteration 1 prompted a change in infill density to strengthen the inner end-fitting, and a print orientation was changed to allow the layer lines to sit in line with the axial load. Inner end-fitting pullout was observed in iteration 2 where the addition of a retaining ring was implemented to hold the component in place. Thread failure occurred in iteration 3, where an increase in shells, a change in printing mode from balanced to solid, and an inner end-fitting extension were incorporated to reduce damage to the threads and add more resistance to an inner end-fitting pullout. The PAM's maximum axial contraction force and burst pressure were increased from 363 lbf at 43 psi to 1160 lbf at 123 psi. The 3D-printed PAM was then characterized in actuation to determine its performance capabilities, which when compared to metallic PAMs, matched axial contraction force and percent contraction at 30, 60, and 90 psi. A slight change in PAM braid angle was taken into consideration when comparing 3D-printed and metallic PAM axial contraction force output.

References

[1] Ryan M. Robinson, Curt S. Kothera, Benjamin K. S. Woods, III Robert D. Vocke, and Norman M. Wereley. High specific power actuators for robotic manipulators. *Journal of Intelligent Material Systems and Structures*, 22(13):1501–1511, 2011.

[2] Ching-Ping Chou and B. Hannaford. Static and dynamic characteristics of McKibben pneumatic artificial muscles. In *Proceedings of the 1994 IEEE International Conference on Robotics and Automation*, pages 281–286 vol.1, 1994.

[3] M. Mori, K. Suzumori, S. Seita, M. Takahashi, T. Hosoya, and K. Kusumoto. Development of very high force hydraulic McKibben artificial muscle and its application to shape-adaptable power hand. In *2009 IEEE International Conference on Robotics and Biomimetics (ROBIO)*, pages 1457–1462, 2009.

[4] Hyun Sung Cho, Tae Hwan Kim, Tae Hwa Hong, and Yong-Lae Park. Ratchet-integrated pneumatic actuator (RIPA): a large-stroke soft linear actuator inspired by sarcomere muscle contraction. *Bioinspiration and Biomimetics*, 15(3):036011, mar 2020.

[5] Robert D Vocke III, Curt S Kothera, and Norman M Wereley. Mechanism and bias considerations for design of a bi-directional pneumatic artificial muscle actuator. *Smart Materials and Structures*, 23(12):125039, nov 2014.

[6] Benjamin K S Woods, Curt S Kothera, Jayant Sirohi, and Norman M Wereley. Pneumatic artificial muscles for trailing edge flap actuation: a feasibility study. *Smart Materials and Structures*, 20(10):105021, sep 2011.

[7] Benjamin K. S. Woods, Curt S. Kothera, and Norman M. Wereley. Wind tunnel testing of a helicopter rotor trailing edge flap actuated via pneumatic artificial muscles. *Journal of Intelligent Material Systems and Structures*, 22(13):1513–1528, 2011.

[8] Benjamin KS Woods, Michael F Gentry, Curt S Kothera, and Norman M Wereley. Fatigue life testing of swaged pneumatic artificial muscles as actuators for aerospace applications. *Journal of Intelligent Material Systems and Structures*, 23(3):327–343, 2012.

[9] Darwin G. Caldwell, N.Tsagarakis, and G.A.Medrano-Cerda. Bio-mimetic actuators: polymeric pseudo muscular actuators and pneumatic muscle actuators for biological emulation. *Mechatronics*, 10(4):499–530, 2000.

[10] Frank Cianciarulo, Jacek Garbulinski, Jonathan Chambers, Thomas Pillsbury, Norman Wereley, Andrew Cross, and Deepak Trivedi. Analysis of an anchoring muscle for pipe crawling robot. In Mato Knez, Akhlesh Lakhtakia, and Raúl J. Martín-Palma, editors, *Bioinspiration, Biomimetics, and Bioreplication XIII*, volume 12481, page 1248108. International Society for Optics and Photonics, SPIE, 2023.

[11] Julie Diani, Bruno Fayolle, and Pierre Gilormini. A review on the Mullins effect. *European Polymer Journal*, 45(3):601–612, 2009.

[12] Erica G Hocking and Norman M Wereley. Analysis of nonlinear elastic behavior in miniature pneumatic artificial muscles. *Smart Materials and Structures*, 22(1):014016, dec 2012.